



Seismic evidence for Earth's crusty deep mantle



Daniel A. Frost^{a,*}, Sebastian Rost^b, Edward J. Garnero^c, Mingming Li^d

^a Earth & Planetary Science, University of California, Berkeley, CA, USA

^b Institute of Geophysics and Tectonics, School of Earth and Environment, University of Leeds, Leeds, UK

^c School of Earth and Space Exploration, Arizona State University, Tempe, AZ, USA

^d Department of Physics, University of Colorado, Boulder, CO, USA

ARTICLE INFO

Article history:

Received 8 October 2016

Received in revised form 17 April 2017

Accepted 19 April 2017

Available online 8 May 2017

Editor: J. Brodholt

Keywords:

seismology
deep Earth
scattering
seismic arrays
mantle dynamics
mantle structure

ABSTRACT

Seismic tomography resolves anomalies interpreted as oceanic lithosphere subducted deep into Earth's lower mantle. However, the fate of the compositionally distinct oceanic crust that is part of the lithosphere is poorly constrained but provides important constraints on mixing processes and the recycling process in the deep Earth. We present high-resolution seismic array analyses of anomalous P-waves sampling the deep mantle, and deterministically locate heterogeneities in the lowermost 300 km of the mantle. Spectral analysis indicates that the dominant scale length of the heterogeneity is 4 to 7 km. The heterogeneity distribution varies laterally and radially and heterogeneities are more abundant near the margins of the lowermost mantle Large Low Velocity Provinces (LLVPs), consistent with mantle convection simulations that show elevated accumulations of deeply advected crustal material near the boundaries of thermo-chemical piles. The size and distribution of the observed heterogeneities is consistent with that expected for subducted oceanic crust. These results thus suggest the deep mantle contains an imprint of continued subduction of oceanic crust, stirred by mantle convection and modulated by long lasting thermo-chemical structures. The preferred location of the heterogeneity in the lowermost mantle is consistent with a thermo-chemical origin of the LLVPs. Our observations relate to the mixing behaviour of small length-scale heterogeneity in the deep Earth and indicate that compositional heterogeneities from the subduction process can survive for extended times in the lowermost mantle.

© 2017 Elsevier B.V. All rights reserved.

1. Introduction

Seismological analyses reveal heterogeneities in Earth's mantle from the surface to the core–mantle boundary (CMB) spanning a wide range of scales. In the upper mantle, seismic tomography shows oceanic lithosphere, on the order of 100s km thick, subducting into the Earth (Grand et al., 1997). The oceanic crust component of the lithosphere is subducted into the mantle at a rate of $\sim 20 \text{ km}^3$ per year at present-day (Li et al., 2016). The crust has been modelled to advect into the lower mantle (Christensen and Hofmann, 1994), and may represent up to 10% of the mass of the mantle from subduction through Earth's history (Hofmann and White, 1982). Geochemical anomalies in ocean island basalts sourced from the deep Earth suggest that oceanic crust is incompletely mixed into the mantle (Stracke et al., 2003). Meanwhile, tomographic images of the lowermost mantle are dominated by two large, 1000s km scale-length, nearly equatorial and antipodal, structures of reduced seismic velocities (e.g. Dziewonski, 1984),

both in S- and P-wave velocity (V_s and V_p , respectively); these are surrounded by zones of higher seismic velocities, which are commonly attributed to cooler subduction-related downwellings. The nature and origin of these LLVPs remains enigmatic but may be related to dense thermo-chemical piles (Garnero and McNamara, 2008) possibly consisting of primordial material (Labrosse et al., 2007), products of chemical reactions with the outer core (Knittle and Jeanloz, 1991), or accumulation of subducted oceanic crust (Christensen and Hofmann, 1994). A purely thermal origin of LLVPs has also been advocated (Davies et al., 2015). Geodynamic models indicate that subduction-related currents shape the thermo-chemical structures into piles that internally convect (McNamara and Zhong, 2005).

Significantly smaller scale heterogeneity has been inferred from high-frequency ($\sim 1 \text{ Hz}$) seismic energy trailing (coda) or preceding (precursors) some seismic waves (Shearer, 2007), due to scattering from volumetric heterogeneities with scales similar to the dominant seismic wavelength (Cleary and Haddon, 1972) (e.g. of order 10 km in the lowermost mantle for 1 Hz waves). While seismic probes differ in their sensitivities to the scale and depth of scattering heterogeneity, scattered waves help to characterise fine scale

* Corresponding author.

E-mail address: dafrost@berkeley.edu (D.A. Frost).

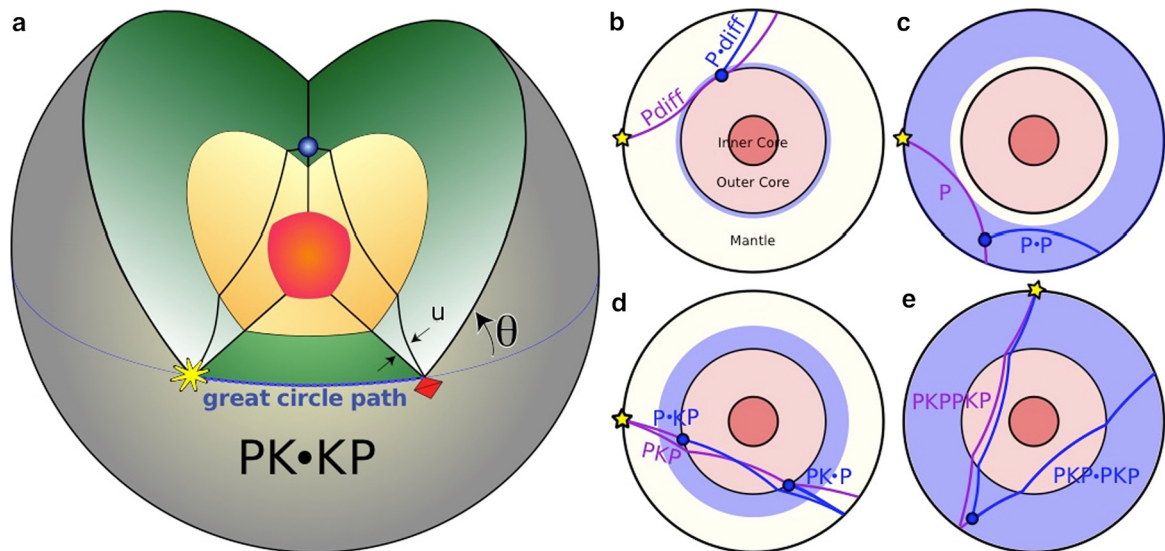


Fig. 1. Raypaths of direct and scattered waves used to map small-scale mantle heterogeneity. (a) PK•KP path from an earthquake (star) to a scattering heterogeneity at or near the CMB (blue dot), and to the array (pyramid). The scattered wave travels out of the great-circle path. Other scattered waves used to study mantle structure include (b) P_{diff} : a P-wave diffracted along the core-mantle boundary (CMB) and back up to the surface. The wave can be scattered at some distance along the diffracted portion, denoted $P_{\bullet\text{diff}}$. Direct and scattered paths (purple and blue lines, respectively), and example scattering location (blue circle) are shown along with the depth range (blue shaded region) that can be studied with this probe. (c) P: a direct P-wave, which can be scattered some depth, indicated by •, to another P wave (or S wave, then called P•S) which travels back to the surface, (d) PKP: a P-wave which travels through the mantle, outer core, and back up to through the mantle the surface. This wave can be scattered within the mantle, the location of which is indicated by •, either before the wave enters the outer core (P•KP), or as the wave exits the outer core (PK•P), (e) PKPPKP: a wave which travels down through the mantle and outer core, up through the mantle and reflects off the underside of the CMB, and returns down through the mantle and up through the outer core and mantle to the surface. A similar wave can be scattered back down through the mantle on the antipodal side and back up to the surface, which can be written as PKP•PKP. (For interpretation of the references to colour in this figure legend, the reader is referred to the web version of this article.)

mantle heterogeneity (Shearer, 2007). The radial dependence of scattering has been investigated with PKP waves (P waves that go through Earth's core), which indicate the presence of weak (e.g., V_p perturbations, dV_p , of 0.1% RMS), small-scale (6–8 km) heterogeneity distributed throughout the mantle (Mancinelli and Shearer, 2013). These studies present global, radially averaged statistically viable scattering populations but are not able to deterministically locate scattering heterogeneities. Upper mantle regional studies of scattered PP and SS waves (Fig. 1), have deterministically mapped scatterers in subduction zones in the upper and mid-mantle, relating the heterogeneities to subduction processes (Kaneshima and Helfrich, 1998). Lower mantle regional studies using PKP have demonstrated regional deep mantle scattering (Frost et al., 2013; Ma et al., 2016) with strong lateral variations. These lowermost mantle heterogeneities have been attributed to a variety of processes including subduction, plumes, melt processes, and phase transitions. Regional geodynamic models of the upper mantle have demonstrated the role of large-scale convection in generating and manipulating heterogeneity across length-scales (e.g. Korenaga, 2004). While scattering scale-lengths have been previously inferred, the data used are typically band-limited or filtered to high frequency, thereby restricting the constraint on the range of scale lengths that can be deduced. Here we present a seismic probe and method for precise location of scattering heterogeneities near the CMB and simultaneous determination of their dominant scale lengths over a wide spectrum of possibilities.

We use a scattered form of PKPP which first propagates as a P-wave through the mantle, into the core, and back up to the lower mantle (as a normal PKP wave), and then is scattered in the lowermost mantle depth shell back into the core, and then travels through the mantle to the receiver (Rost and Earle, 2010). We refer to this scattered path as PK•KP, where the dot “•” represents the small portion of the path travelled as P-wave from the CMB up into the lower mantle to the scattering location, then back to the CMB. PK•KP may involve out-of-great circle plane scattering and travel along asymmetric source and receiver paths (Fig. 1).

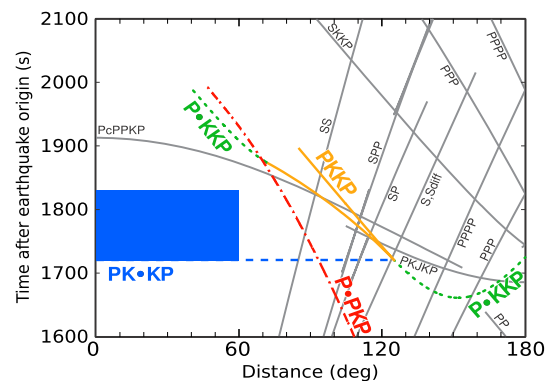


Fig. 2. Travel-time curves of PK•KP and related scattered waves. In the study we use data with source-receiver distances between 0 and 60 degrees and from the first theoretically viable arrival of PK•KP to 110 s after (blue box). Times of other variants of the PKPP path (coloured lines) are also shown (See Earle, 2002 for discussion of other scattered phases). Times of non-scattered waves are shown as grey lines. The blue dashed line depicts PK•KP times at larger distances, which are not used here due to interference with other arrivals. All travel time curves are calculated using IASP91 (Kennett and Engdahl, 1991) and a surface focus earthquake. Figure after Earle (2002). (For interpretation of the references to colour in this figure legend, the reader is referred to the web version of this article.)

This probe is especially suited for studying lower mantle heterogeneities because PK•KP arrives in a quiet time-distance window for teleseismic data (Fig. 2), it avoids the source-receiver CMB location ambiguity of PKP scattering (Fig. 1d), it allows deterministic identification of the heterogeneity location, and it allows sampling of an extensive volume of the Earth's mantle (Fig. 3).

2. Data and array-processing methods

While past work introduced the feasibility of this phase for deep mantle heterogeneity detection, analysis was limited geographically and in depth (Rost and Earle, 2010). We collect earthquakes with magnitudes larger than 6.0 occurring in a 17-year period (1995–2012) within 0-to-60° epicentral distance from 13

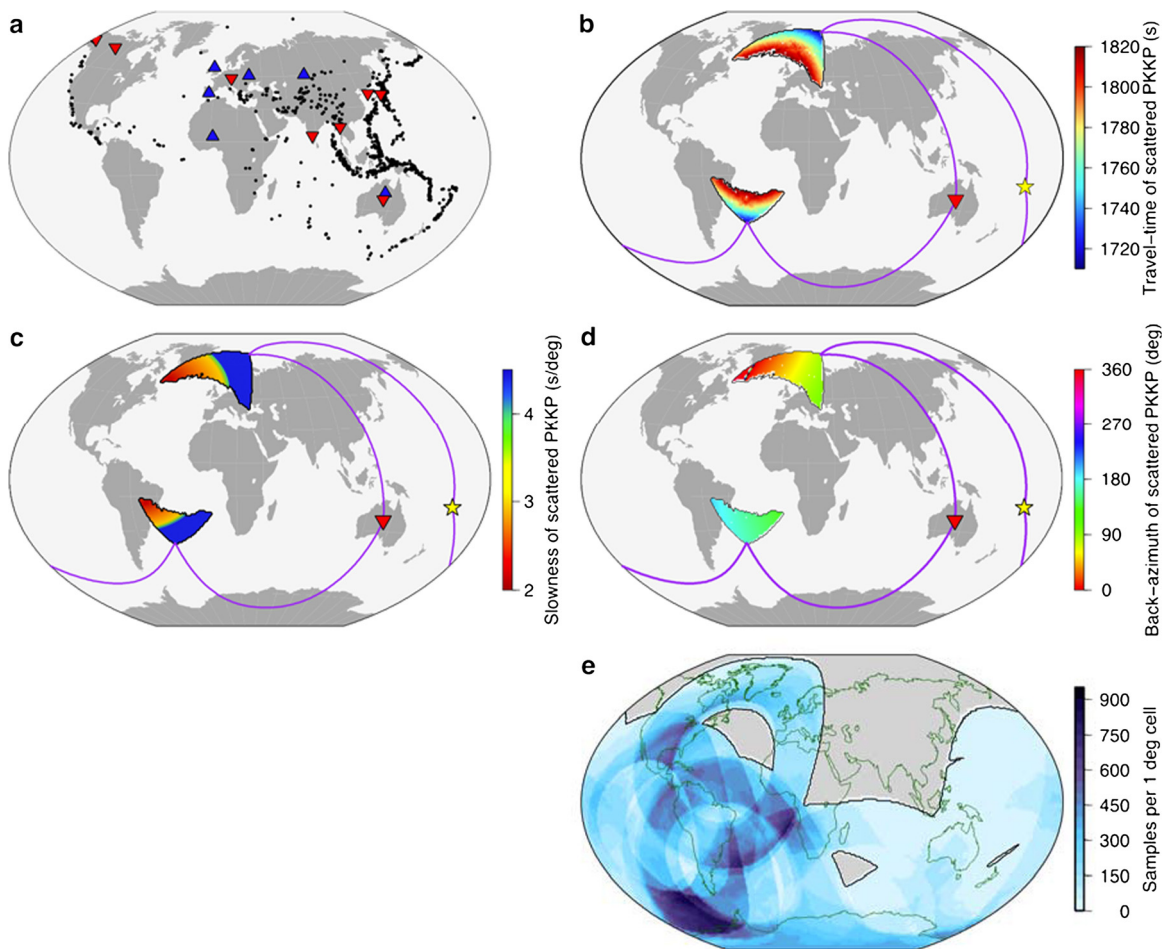


Fig. 3. Data and resultant sampling of the lower mantle by PK•KP. (a) 1095 events (black dots), and 6 broadband (blue triangles) and 8 short-period (red triangles) arrays used. For a given source (yellow star) and receiver array (inverted red triangle), the regions of possible scattering can be predicted along with the associated (a) travel-time, (b) back-azimuth, and (c) slowness of a PK•KP wave scattered at the CMB at each point in the sampled region. Example ray paths from the source to both scattering regions (on either side of the inner core) and back to the array are predicted and displayed as purple lines. (e) Sampling of CMB by PK•KP for the source and receiver distribution in (a) calculated by super-position of potential scattering regions as in (c). Black line outlines region sampled by this dataset. (For interpretation of the references to colour in this figure legend, the reader is referred to the web version of this article.)

International Monitoring System (IMS) arrays and the Gauribidanur array in India (Fig. 3). While PK•KP could feasibly be observed at greater distances, the upper distance limit was imposed to avoid possible contamination from other core waves (Fig. 2). Some earthquakes were detected by multiple arrays, resulting in 2355 earthquake–array pairs from 1095 earthquakes. Every source–array pair allows detection of energy related to multiple scattering heterogeneities. This dataset samples 78% of the surface area of the CMB and lowermost mantle (Fig. 3e), including the southern hemisphere, which was poorly sampled in previous studies and provides us with the to-date best sampling for lower mantle heterogeneity.

Small aperture seismic arrays are effective for deep Earth studies, enhancing low amplitude, yet coherent energy, relative to incoherent background noise. We analyse a 110 s time window following the first theoretical PK•KP arrival, allowing investigation of scattering within the lowermost 320 km of the mantle. To identify scattered signals and determine the slowness (u), back-azimuth (θ , measured relative to the great circle path between the earthquake and the array), and arrival time of incoming signals we analyse data using a frequency-wavenumber (fk) approach (Capon et al., 1967), in addition to using the F -statistic (described below). While other high-resolution processing schemes are available, fk-analysis was selected for its increased computational speed over traditional beam-forming and Vespa (velocity spectral analysis) approaches (Davies et al., 1971). Also, the F -statistic effectively

suppresses aliasing and is applicable to a wide variety of array configurations (Selby, 2008). The data are windowed in time, transformed into the frequency domain, and filtered between 0.5 and 2 Hz. The power spectral density, $S(\omega)$, is then calculated within a given range of incoming directions, which are combined into a single wavenumber vector, k . The fk method collapses the time information to a single point around which the data were windowed. Thus, we adopt a sliding window approach, selecting 10 sec long windows of data (starting from 10 sec prior to the predicted first arrival of PK•KP), applying a cosine taper, and shifting the window in 1 sec steps through the whole PK•KP time range (blue box in Fig. 2), to measure the power of incoming energy from different directions through time.

To increase the resolution of the measured slowness and back-azimuth of PK•KP signals received at the arrays, we apply the F -statistic (Equation 1. Blandford, 1974). This method involves first beaming data on a specific slowness and back-azimuth, dividing the sum of the differences between the beam, b , and each trace in the beam, x_i , within a given time window, M , by the amplitude of the beam within the same window, and then weighting the output by the number of traces, N . This produces a dimensionless number, F , representing the signal coherence by measuring the cumulative difference from the beam at a given time.

$$F = \frac{N-1}{N} \frac{\sum_{t=1}^M b(t)^2}{\sum_{t=1}^M \sum_{i=1}^N (x_i(t) - b(t))^2} \quad (1)$$

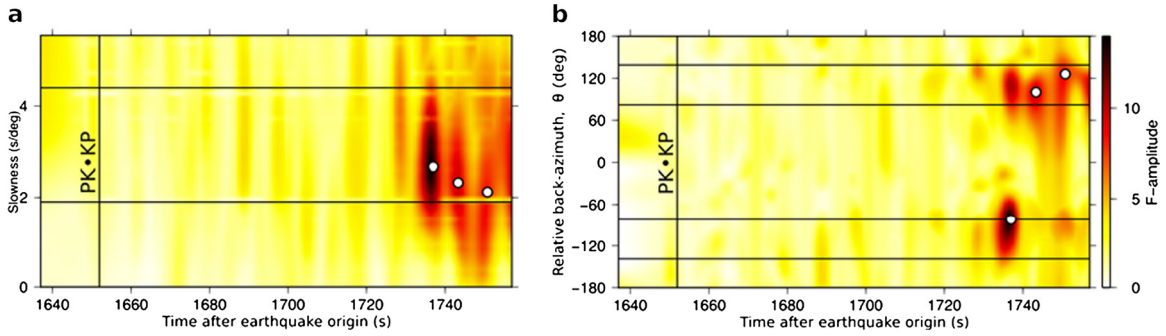


Fig. 4. Array processed PK•KP waves. For a single example event, energy in the PK•KP time window, is *fk* processed, and displayed in terms of (a) slowness and time and (b) back-azimuth (relative to the great-circle path) and time, shown as *F*-amplitude. Three coherent and distinct PK•KP signals are identified (circles). Vertical line marks the first possible PKKP arrival (Fig. 2). Horizontal lines mark the possible range of PK•KP, (a) slownesses (Fig. 3c) and, (b) back-azimuths on both sides of the great-circle path (Fig. 3d).

The *F*-statistic is efficient method of determining the best-fitting slowness and back-azimuth for a given signal in a beam. The method assesses the difference between the waveshape of each trace forming the beam and the beam itself, thus the method heavily penalises beams that differ from the traces used to form that beam. Effectively, this suppresses signals misaligned due to deviations from signal slowness and backazimuth (Selby, 2008). This leads to an increase of the slowness and back-azimuth resolution using small-aperture arrays. This calculation is repeated in a sliding time window to create an *F*-trace, which displays the coherence along the beam.

3. Results

We detect 1989 signals, each associated with an individual scattered wave. Fig. 4 presents an example earthquake showing energy from several heterogeneities. The amplitude of scattered PK•KP waves is very low, often close to the noise level, thus array processing is necessary to clearly resolve these signals. We are unable to determine the relative amplitude of the PK•KP waves, as there is no suitable reference phase for each scatterer with a similar path.

Using the geometrical direction of scattered arrival information (u, θ) to constrain the path from scatterer to receiver (•KP) in combination with the timing information (t), which indicates the length of the whole path, we determine the locations of the scattering heterogeneity in terms of latitude, longitude, and depth, by ray-tracing from the seismic array through a 1-dimensional Earth model (IASP91, Kennett and Engdahl, 1991). A 2-dimensional grid of distance from the array and height above the CMB is constructed representing possible scattering locations of PK•KP, oriented in the direction of wave propagation along the back-azimuth observed at the array. The whole PK•KP path can comprise any combination of either the ab or bc branches of PKP. We ray-trace to and from each point in the grid along PKd and dKP paths, respectively, where the “d” represents the depth of scattering in the lower mantle. For each distance and each scattering depth in the grid, all permissible combinations of down-going PK_{abd} or PK_{bcd} legs and up-going dKP_{ab} or dKP_{bc} legs are considered.

Each of the PK_{abd} and PK_{bcd} branches has different, yet partially overlapping, distance ranges (which vary as a function of depth, d , of the scattering heterogeneity). The grid is formed for the distance range of the PK_{abd} and PK_{bcd} paths, and heights from the CMB to 300 km above into the mantle. To maximise processing speed and accuracy, a coarsely spaced grid is first searched (constructed with 40 km depth intervals and 4° distance intervals) between the CMB and 300 km above, followed by the finer grid projected ± 50 km from the best-fitting point in the coarse grid with 10 km depth intervals and 0.5° distance intervals, thus allowing scatterers to be located up to 350 km above the CMB.

Each complete path from the source to each point in the scattering grid and up to the surface is associated with a travel-time (the sum of the down-going and up-going legs) and slowness (of the up-going leg to the seismic array). From these possible paths, we find the best fitting scattering distance, depth, and complete path branch combination by minimising the residual between slowness and travel-time of the traced ray and the observed slowness and travel-time. The minimisation process is weighted in favour of picking the smallest possible slowness residual (relative to the observed value) as it controls scattering location more strongly than does travel-time, meaning that for anomalies of similar magnitudes (e.g. 1 s/deg slowness and 1 s travel-time) the slowness anomaly affects scattering location more significantly than does the travel-time anomaly.

Of the signals initially identified in the *fk* analysis, those with slownesses or back-azimuths incapable of producing viable PK•KP paths are discarded (508 signals). For signals whose observed slowness and time can be matched to that of a PK•KP scattering location, we retain the best fitting scattering point identified in the second grid iteration. The misfit between the slowness and time of the best fitting ray and that observed in the data (with the *fk* *F*-statistic) is used to assess the quality of the scatterer solution location: scatterers are disregarded if either the slowness misfit is greater than 1.5 s/deg, the travel-time misfit is greater than 2.5 s, or if the *F*-amplitude (coherence) of the scattered signal is more than twice that of the P-wave signal for the same event. For the latter, we assume the direct P-wave measured on the minor arc should be considerably more coherent than the scattered PK•KP energy. These mislocation ranges were determined from analysis of synthetic signals calculated for the geometry of each array in this study. This resulted in discarding 534 additional signals. This analysis does not include consideration of the sub-array structure, but the influence of this is likely small for the majority of the arrays in our study (Bondar et al., 1999). Therefore, we twice discard data, firstly if the observed back-azimuth and slowness cannot trace a viable PK•KP path, and secondly if the misfits between the traced and observed slowness and time or the *F*-amplitude are above a threshold (1042 total signals discarded), leaving 947 signals traced to scattering heterogeneities in the deep mantle. The combined uncertainties in u , θ , and t yield a mislocation range in the mapped scattering heterogeneity locations up to ± 150 km laterally and ± 30 km vertically.

4. Frequency analysis

Six of the arrays used contain broadband sensors (Table S1). For these data (113 signals) we investigate the spectral character of scattered energy by calculating the scattering strength in seven different octave wide band-pass filters from 0.25 to 32 Hz.

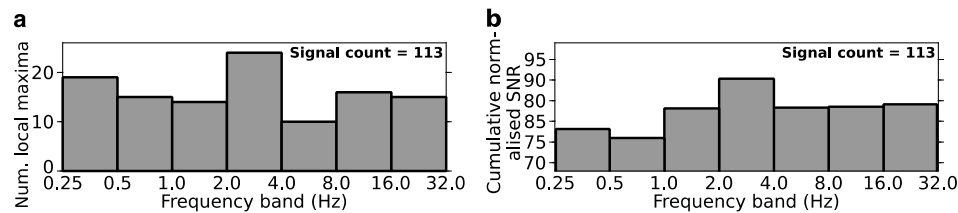


Fig. 5. Frequency characteristics of 113 PK•KP waves observed at the 6 broadband arrays displayed as, (a) strongest Signal-to-Noise-Ratio (SNR) (each signal contributes 1 to count) and, (b) cumulative SNR (each signal normalised to one before summing).

We calculate the signal-to-noise ratio (SNR) by comparing the amplitude of the linear beam of scattered energy (created using the observed slowness and back-azimuth of that signal) to the noise (from the same beam) that precedes the predicted first possible PK•KP arrival. Across these events, we observe a spectrum of scattered energy between 1 and 32 Hz (indicating heterogeneity scales at the base of the mantle spanning 0.4–14 km) with the strongest scattered energy most commonly observed in the 2 to 4 Hz frequency band (Fig. 5), equivalent to 4–7 km heterogeneity size and consistent with heterogeneity scales found recently by modelling PKP precursors (Mancinelli et al., 2016). Scattered energy is found across the spectrum indicating that heterogeneities of a large range of sizes exist in the lowermost mantle. While beam forming may act as a mild low-pass filter, the overall spectral content of our beamed and unbeamed data show little difference. Thus, beam-forming can be effectively used to align and sum the coherent PK•KP signals resulting in their emergence from the background incoherent noise. Any small changes to the spectral content caused by the beam-forming process will affect both the scattered signals and the noise to which it is measured relative. Plots of the spectra of the scattered energy calculated from individual records do not reveal the scattered signals due to their very small amplitude relative to the noise level.

To confirm the assumption that scattered energy in the 2 to 4 Hz frequency range is indicative of heterogeneities from 4 to 7 km in size, we model the scattered PK•KP energy generated in different frequency bands for point heterogeneities with an 8 km correlation length using an exponential representation of the heterogeneity spectrum. We model the scattered energy using a Monte Carlo, Phonon Scattering code (Shearer and Earle, 2004) that maps the passage of particles representing seismic energy, or phonons, from a source through a 1-dimensional velocity structure along a range of ray parameters (take-off angles). The synthetic seismic wavefield is constructed by accumulation of phonons across distance and through time. The 1-dimensional velocity structure can be augmented with addition of layers of heterogeneity, which may cause waves passing through the layer to scatter. The velocity and scattering structure is 1-dimensional but the algorithm takes off-Great Circle Path scattering into account, thus this method can model PK•KP paths. However, as the scattering structure is uniform laterally, this method cannot be used to accurately model the observed scattered signals that are generated by unevenly distributed structure. Nonetheless, the method is an effective way to assess the effects on the scattered wavefield of varying the depth distribution, elastic parameters, or scale-length of scattering heterogeneity, as well as the incident seismic wave frequencies (Mancinelli and Shearer, 2013; Mancinelli et al., 2016). Using a different autocorrelation function to describe the heterogeneity spectrum would likely have a small influence on the resultant scattered energy.

We utilise the above method to construct a model with scattering heterogeneities in the lowermost ~300 km of the mantle, consistent with the depth range that we are able to study with our data. Heterogeneities have an RMS velocity perturbation of 0.5%, and a scale-length of 8 km. We simulate the scattered wavefield

at different incident frequencies (effectively bandpass filtering the scattered signals): 0.25, 0.5, 1, 2, 4, 8, 16, and 32 Hz. We find that at lower frequencies up to 1 Hz, scattering in the PK•KP time window is sporadic and weak (Fig. 6). At 1 Hz, scattering becomes more prominent. However, scattering is strongest and most consistent at frequencies from 2 to 4 Hz indicating that scattering from heterogeneities 8 km in size would be most strongly observed at these higher frequencies. At 8 Hz and above scattered signals very rapidly become weak, seven orders of magnitude lower amplitude than at 4 Hz. Above 8 Hz scattered waves are absent from the synthetics. The relatively smooth envelope of the scattered energy results from the 1-D nature of the model. The amplitude of scattered energy increases through time as the PK•KP wave interacts with a greater lateral and vertical extent of the mantle, expanding from a scattering point on the CMB at 1710 s after the origin.

4.1. Distribution of scattering heterogeneities and mantle structures

We investigate the relationship between the abundance of scattering heterogeneities and the large-scale seismic structures in the lower mantle as resolved by seismic tomography. To remove sampling bias from our scattering population due to uneven event-array distributions, we normalise the scattering population by the geographic distribution of scattering (Fig. 3e). The resulting normalised scattering distribution indicates laterally uneven heterogeneity distributions, which cannot be explained by the sampling (Supplementary Fig. 1). We analyse the spatial correlation between the locations of scattering heterogeneities and regions of (1) high or low tomographic velocity anomalies and (2) high or low lateral velocity gradients across the CMB for seven recent S-wave tomographic models: GyPSuM (Simmons et al., 2010), HMSL-S06 (Houser et al., 2008), savani (Auer et al., 2014), SEMUCB-WM1 (French and Romanowicz, 2014), S362WMANI + M (Moulik and Ekstrom, 2014), S40RTS (Ritsema et al., 2011), and TX2011 (Grand, 2002) (Figs. 7 and Supplementary Fig. 2) and for 4 recent P-wave tomographic models: GAP_P4 (Obayashi et al., 2013), GyPSuM_P (Simmons et al., 2010), HMSL_P06 (Houser et al., 2008), and MIT-P08 (Li et al., 2008) (Fig. 8 and Supplementary Fig. 2). While the scattering heterogeneities are observed using P-waves, we compare our results to S-wave tomography models from which LLVPs are defined.

We first distinguish regions related to subduction (positive dVs), and the LLVPs (negative dVs). For each model, we calculate lateral velocity gradients ($\nabla(dVs)$) measured over a horizontal distance of 10° . This gradient distance results in regions of high velocity gradient consistent with the outline of the LLVPs as observed by high-resolution forward modelling studies (He and Wen, 2009).

We compare the distribution of velocity perturbations and gradients against the normalised scattering heterogeneity distribution. As the magnitude, range, and precise pattern of velocity anomalies varies between tomography models, we are unable to select single values of dVs or $\nabla(dVs)$ that are suitable for defining LLVP boundaries for all models. To standardise comparisons of our scattering heterogeneity distribution and the different tomographically derived LLVPs, we compare to specific percentage areas of the

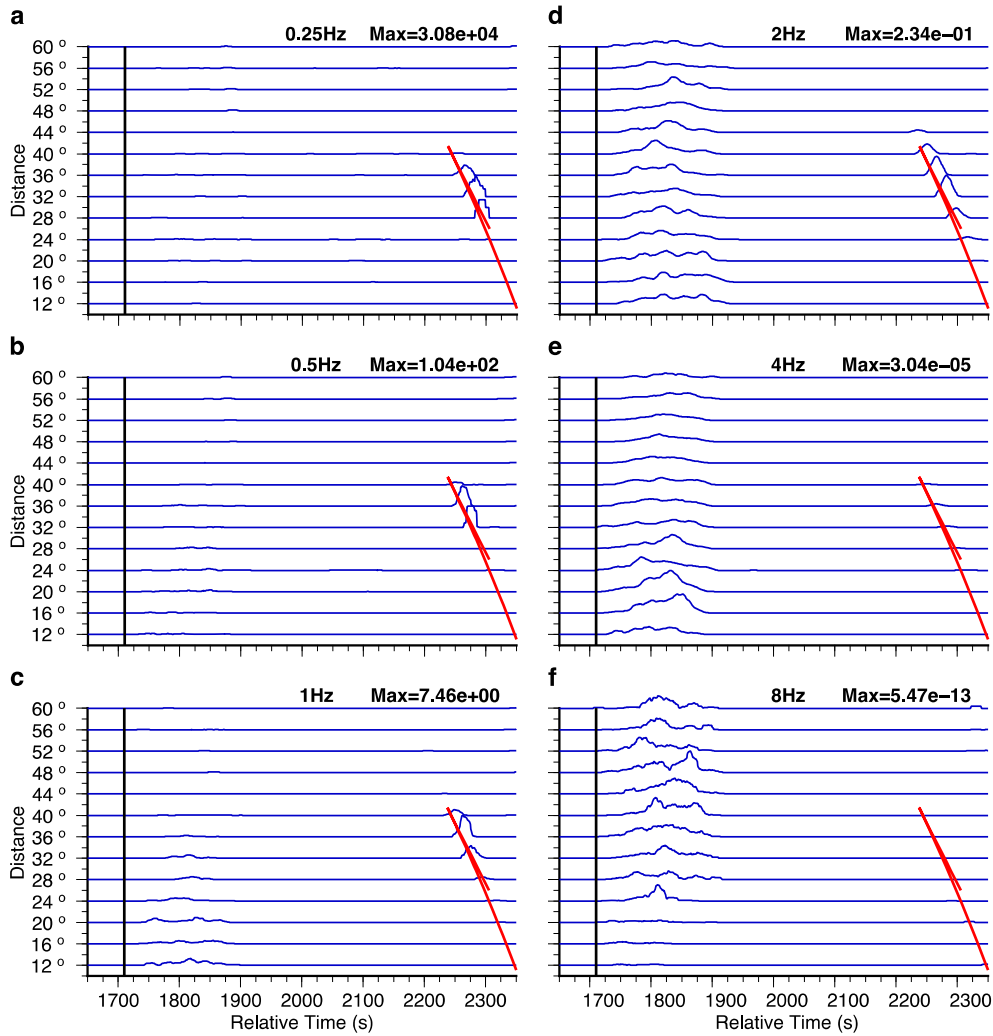


Fig. 6. Synthetic scattering model of a 1-dimensional Earth probed at different frequencies. A Monte Carlo method (Shearer and Earle, 2004) treating waves as packets of energy (phonons) is used to build a synthetic wavefield including scattering at incident frequencies of (a) 0.25, (b) 0.5, (c) 1, (d) 2, (e) 4, (f) and 8 Hz. Phonons sample a 1-dimensional Earth model with a 290 km thick layer in the lowermost mantle containing scattering heterogeneities with an RMS velocity perturbation of 0.5%, with correlation lengths of 8 km. We model a range of distances comparable to our data, and display envelopes of the smoothed sum of wavefield profiles in a ± 2 degree distance range about the central distance. For each frequency, all profiles are normalised to the maximum of the profile at 32° (shown at the top right) to account for the amplitude at the P3KP caustic, the arrival of which is marked in red. The black line marks the expected onset time of PK•KP scattering.

CMB occupied by high or low velocity or gradient (Supplementary Fig. 5). We calculate the number of scattering heterogeneities, as a proportion of the total population of scatterers, within a range of values of velocity anomaly, calculated by the CMB area (5, 10, 15, 20, 25, 30, 40, 50, 60, 70, 80, 85, 90, and 95% area of highest or lowest velocity or gradient anomalies).

We assess the statistical significance of these correlations by comparing them with the spatial correlation between randomly rotated tomographic models and the scattering dataset (Supplementary Figs. 3 and 4). Each tomography model is rotated (through random co-latitude and longitude angles) and the correlations with scattering heterogeneities are recomputed. This is repeated 100 times for each model. The significance of correlations between scatterer locations and actual locations of tomography features is determined by comparison with the distribution of correlations with the randomly rotated tomography models. When correlation of the scattering distribution with the original, unrotated models are fully or dominantly outside of the range calculated for with randomly rotated models (defined by 1 standard deviation, shown as grey shaded regions in Figs. 7 and 8), we conclude the relationship to be statistically significant. We observe a statistically robust increased concentration of scattering heterogeneities in regions of

the highest lateral velocity gradients (Fig. 7c) and a weak correlation between scattering heterogeneities and low velocity anomalies (Fig. 7e), the former are associated with the edges of the LLVPs (Thorne et al., 2004).

When reviewed more closely, we find that scattering heterogeneity shows the strongest correlation with moderately low velocities (~ 20 – 40% of CMB area occupied by lowest velocities). This correlation is most prominent with P-wave models (Supplementary Figs. 2 and 3). Meanwhile, the correlation with lateral gradients is highest for the very strongest gradients. Both moderately reduced velocities and high gradients characterise the boundaries of the LLVPs.

4.2. Distribution of scattering heterogeneity and geodynamic models

We explore geodynamical calculations of subducted oceanic crust entrained into mantle flow in a model where the lower mantle contains chemically distinct thermochemical piles. We model flows in the mantle with a 2-dimensional Cartesian numerical convection calculation, which solves the conservation equations of mass, momentum, and energy in Boussinesq approximation (Li et al., 2014) using the CitCom code (Moresi and Gurnis, 1996). Our

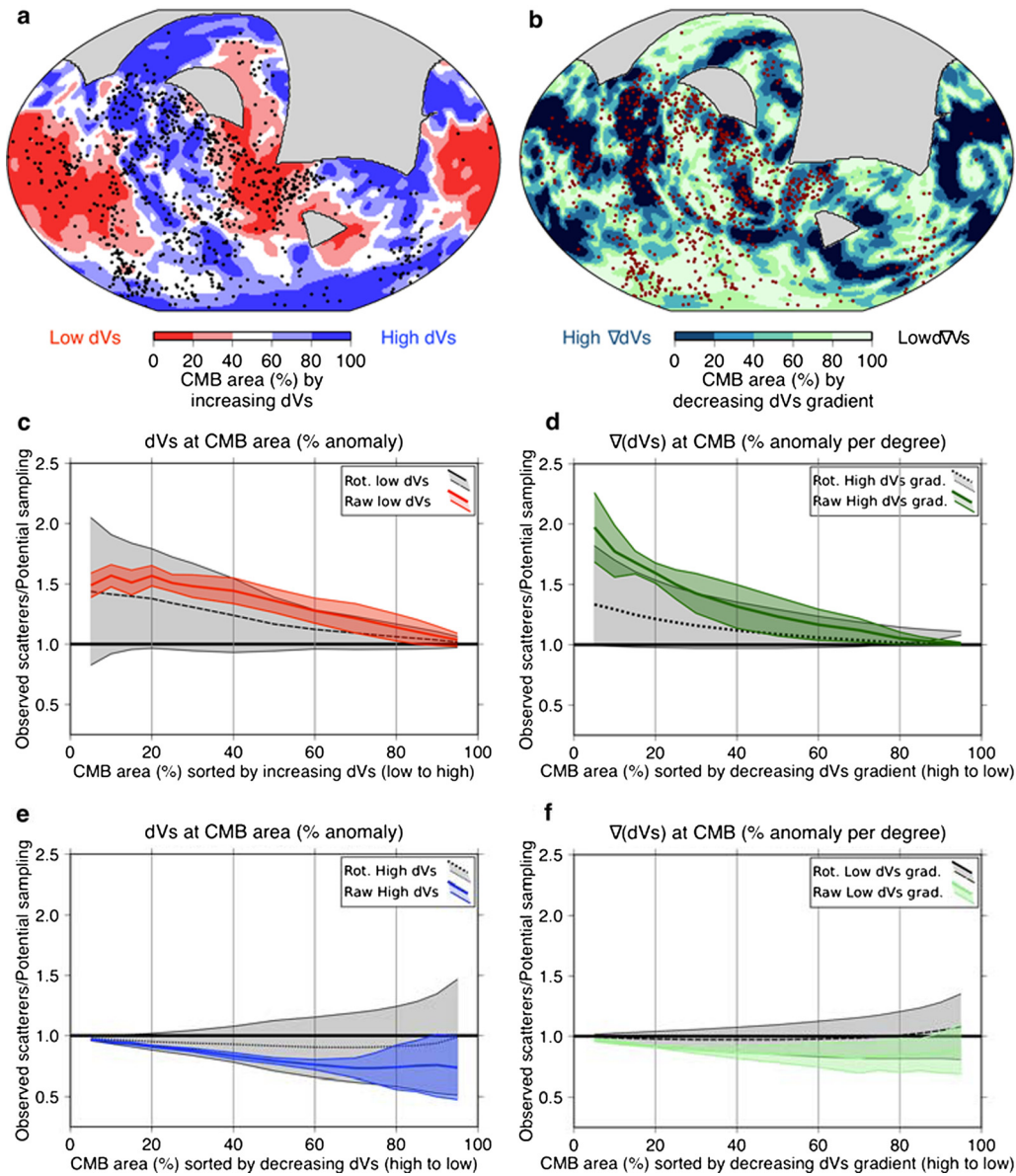


Fig. 7. Correlation of scattering heterogeneities with large-scale S-wave seismic structure. Percentage area of the CMB covered by (a) S-wave velocity anomalies increasing from low to high, and (b) lateral velocity anomaly gradients decreasing from high to low (S40RTS, Ritsema et al., 2011). Scattering heterogeneities are shown as dots. The highest gradients in (b) match well the edges of LLPVs seen in the tomography map, (a) where the magnitude of the velocity anomaly changes rapidly. Ratio of observed to potential scatterers against (c) increasing velocity anomaly (red lines), (d) decreasing lateral velocity gradient (dark green lines), (e) decreasing velocity anomaly (blue lines), and (f) increasing lateral velocity gradient (light green lines). The black horizontal line indicates a 1-to-1 ratio of sampling-to-scattering, data above and below this line indicate more or fewer heterogeneities than expected based on sampling, respectively. Displayed is a compilation of the correlations with 7 tomography models shown by the mean and 1 standard deviation (thick coloured lines and shading, respectively) (Supplementary Fig. 3 shows individual analysis). Correlations are also calculated for random rotations of the 7 models (black lines and grey regions for mean and standard deviation, respectively). Tomographic anomalies are displayed by CMB area, sorted by anomaly magnitude. (For interpretation of the references to colour in this figure legend, the reader is referred to the web version of this article.)

model contains three compositional components, including ambient mantle, denser pile material, and oceanic crust. The density for each compositional component is the same as the reference case of Li et al. (2014): the oceanic crust and pile material have the same non-dimensional buoyancy number of 0.8 ($\sim 2\text{--}3\%$ denser than the ambient mantle). The Rayleigh number is $Ra = 1 \times 10^7$. The temperature dependent viscosity is given by $\eta_T = \exp[A(0.5 - T)]$, with activation coefficient $A = 9.21$, resulting in four orders of magnitude variations of viscosity due to changes of temperature. We employ a viscosity increase by a factor of 50 from upper mantle to lower mantle at 660 km depth. In addition, a phase transition from bridgmanite to post-Perovskite acts to reduce the viscosity in colder regions of the lowermost mantle. All boundaries are free-slip. The upper and lower surfaces are isothermal

while the sides are insulating. The advection of the composition field is simulated by tracers. A 6 km thick oceanic crust is introduced on the surface of the model by setting the identity of tracers shallower than 6 km depth to crust, and the oceanic crust is later subducted into the deep mantle. We analyse the evolving distribution of crustal tracers with respect to the dense primordial piles in the lowermost part of the model close to the CMB (Fig. 9). While some studies of the dynamic behaviour of heterogeneities are able to analyse the evolution of their shape (e.g. Olson et al., 1984), by treating heterogeneities as tracers we are unable to determine the nature of the mechanical mixing (stretching and folding) of initially planar collections of tracers that represent the crust. For a full description of the modelling procedure employed here see Li et al. (2014) and supplementary information therein.

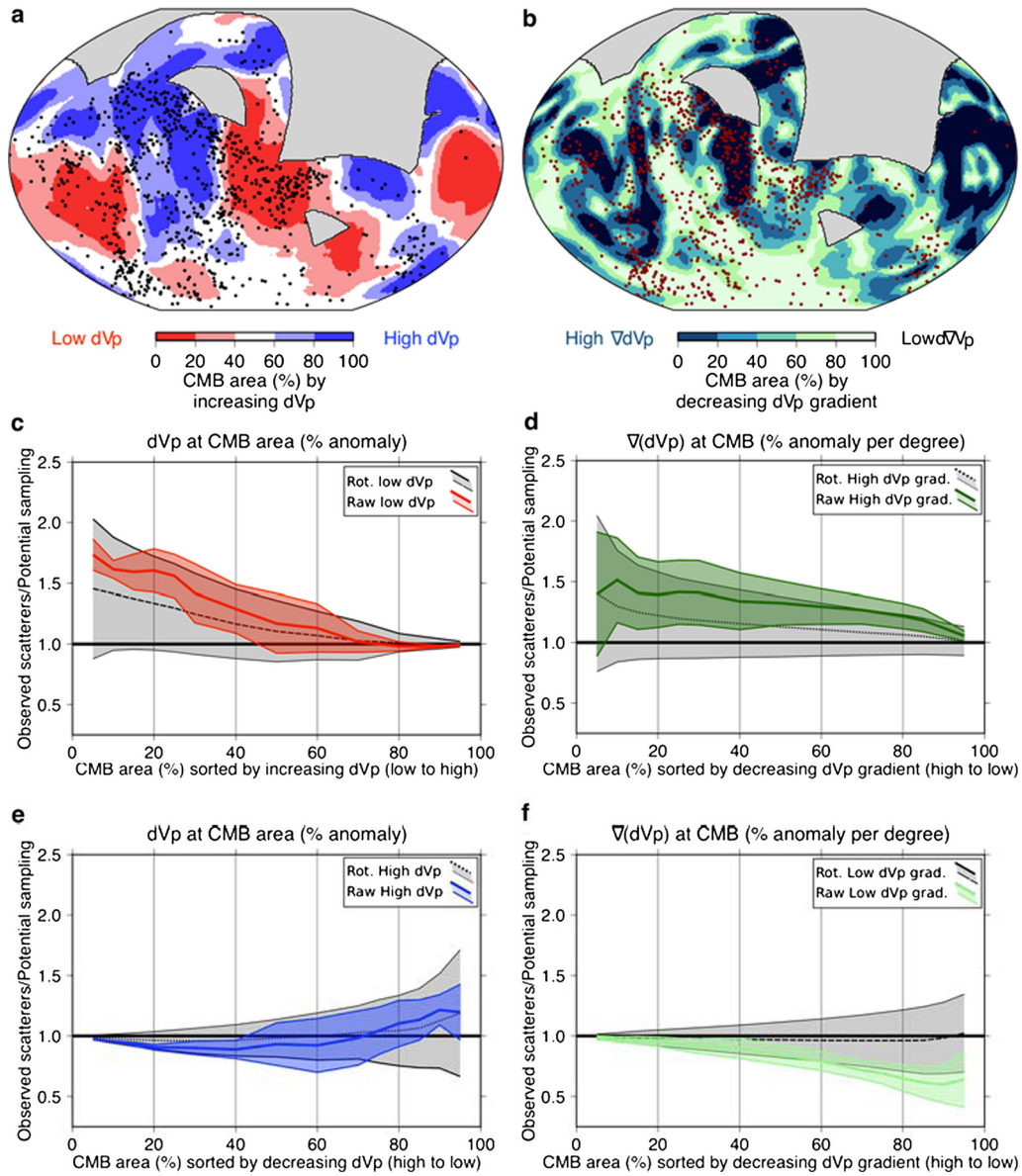


Fig. 8. Correlation of scattering heterogeneities with large-scale P-wave seismic structure. Percentage area of the CMB covered by (a) P-wave velocity anomalies increasing from low to high, and (b) lateral velocity anomaly gradients decreasing from high to low (GAP_P4, Obayashi et al., 2013). Scattering heterogeneities are shown as dots. Ratio of observed to potential scatterers against (c) increasing velocity anomaly (red lines), (d) decreasing lateral velocity gradient (dark green lines), (e) decreasing velocity anomaly (blue lines), and (f) increasing lateral velocity gradient (light green lines). The horizontal line indicates a 1-to-1 ratio of sampling-to-scattering, data above and below this line indicate more or fewer heterogeneities than expected based on sampling, respectively. Displayed is a compilation of the correlations with 7 tomography models as the mean and 1 standard deviation (thick coloured lines and shading, respectively) (Supplementary Fig. 4 shows individual analysis). Correlations are also calculated for random rotations of the 7 models (black lines and grey regions for mean and standard deviation, respectively). Tomographic anomalies are displayed by CMB area, sorted by anomaly magnitude. (For interpretation of the references to colour in this figure legend, the reader is referred to the web version of this article.)

In this model, subducted crust has an elevated concentration near the boundaries of the thermochemical piles due to the change in flow direction from lateral (between piles) to radial (vertically along pile margins). The edges of the modelled thermochemical piles display high temperatures, and also high thermal gradients across the margins (Li et al., 2014). The high concentration of oceanic crust along the pile edges in these simulations (Fig. 9) thus matches seismic observations showing increased concentration of scatterers in regions of low seismic velocity and high velocity gradients (Fig. 7). The distribution of crustal remnants near pile margins is time dependent, due to the subduction-related flow patterns, but agrees well with our observations over many time snapshots and different locations (Supplementary Figs. 5 and 6). In this model there is initially no crust and the mantle, but the amount of crust increases through time, dependent on the rates

and densities chosen. As such, the model cannot be used to compare relative quantities of the three compositions. We find that the general patterns of crust distribution in the models qualitatively match our observations. In addition, the oceanic crust can be entrained in to thermochemical piles (Li et al., 2014), which may cause seismic scattering within LLVPs.

5. Discussion and conclusions

Past work has investigated how shallow structure beneath seismic arrays can affect the resolved direction of incoming seismic waves (Bondar et al., 1999). In our analysis, we dominantly use arrays that have previously been demonstrated to have minor or insignificant sub-surface structure. Not all arrays used here have calculated slowness-azimuth station corrections, and calculating

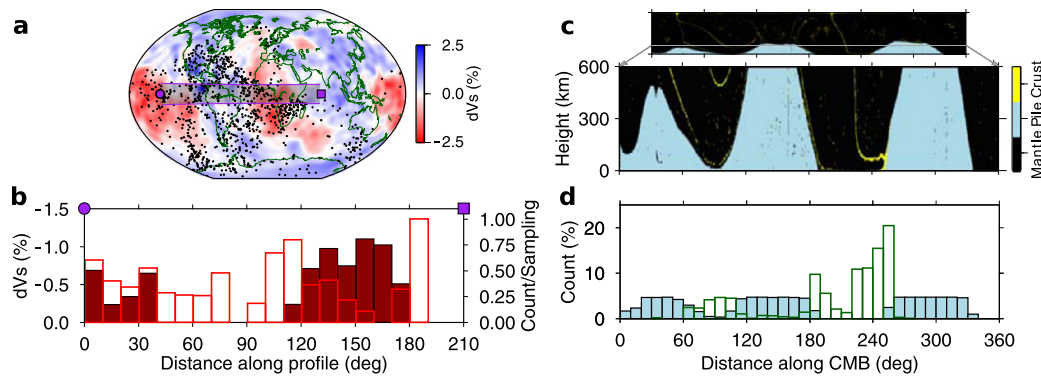


Fig. 9. Scattering heterogeneities, crust, and thermochemical pile margins. (a) Velocity anomalies at CMB (S40RTS, Ritsema et al., 2011), scattering heterogeneities (dots), and a 20° wide cross-section swath from 140°W, 0°N to 70°E, 0°N (shaded). (b) Normalised ratio of observed to potential scatterers along the cross-section (open bars, right legend, maximum = 2.08×10^{-4}), and tomographic velocity reductions averaged across swath, indicating LLVPs (closed bars, left legend). (c) A time snapshot from numerical thermo-chemical convection calculation (Li et al., 2014) displaying distribution of tracers representing crustal (yellow), pile (blue), and background mantle (black) material in lowermost 600 km of mantle with 10-times vertical exaggeration and whole mantle to scale in upper panel. Tracers are discretized into 10×10 km cells and the dominant tracer defines the cell type (crust, pile, or mantle). (d) Lateral distribution of crust (green bars) and thermo-chemical piles (blue bars) in the lowermost 300 km for the time snapshot in (c). (For interpretation of the references to colour in this figure legend, the reader is referred to the web version of this article.)

these for all arrays is beyond the scope of this paper. Nonetheless, when we remove the data from Chiang Mai array, which shows the largest station corrections (which accounts for of the 20% of the well-resolved scattering locations), there is no notable change in the correlations with the tomographic structures, thus the observed correlations are defined by results from other arrays with less influential sub-surface structure.

The dominance of 2 to 4 Hz energy in the scattering spectrum (Figs. 5) indicates the presence of dominant heterogeneity scale lengths in the deepest mantle of ~ 4 to 7 km. Relatively high thermal conductivity in the lowermost mantle (Hofmeister, 1999) should lead to fast thermal equilibration of small-scale heterogeneities (Olson et al., 1984) suggesting a compositionally distinct origin from the background mantle. The 4 to 7 km scale size agrees well with the thickness of oceanic crust (~ 6 km) and the spacing of normal faults related to slab bending at oceanic trenches (Masson, 1991). The fine-scale heterogeneity mapped here, therefore, may be related to convectively driven segmentation of the formerly contiguous layer of subducted oceanic crust and shows little evidence for strong deformation through viscous forces in the mantle convection (Tackley, 2011).

Other sources of heterogeneity within the lowermost mantle can feasibly produce scattering. LLVP thermochemical pile material can be entrained into mantle flow (Williams et al., 2015), however this does not explain scattering observed within LLVPs. Small scale CMB topography could scatter waves (Doornbos, 1978), but generating wide out-of-great-circle plane PK•KP paths by underside CMB reflections would require unrealistically steep and high amplitude topography at CMB scattering locations to get energy back to the array. Additionally, topography could not explain travel times of signals used to map scattering higher above the CMB. Heterogeneities undergoing the phase transition from bridgmanite (perovskite) to post-perovskite (pPv) (Murakami et al., 2004; Oganov and Ono, 2004) may have locally sharp velocity contrasts. However, the range of meta-stability, where pPv would coexist and thus contrast with bridgmanite, is measured to be 70–600 km thick (Grocholski et al., 2012), below which pPv would be ubiquitous and not provide an elastic contrast, and above which it would not exist, thus this hypothesis would struggle to explain the observed depth range of scattering. Furthermore, pPv is not expected to be stable within the relatively hot LLVPs, thus may not be responsible for scattering in these regions, although there have been limited observations of discontinuities within the LLVPs (Lay et al., 2006). Ultra low velocity zones (ULVZs) are observed to have distinct velocities and densities and may comprise partial

melt or products of chemical reactions between mantle and core material (Williams and Garnero, 1996; Knittle and Jeanloz, 1991). While this material can provide a sufficiently sharp elastic contrast, ULVZs, with thicknesses of only a few 10 s of km, are unable to explain scatterer locations away from the CMB. The increased density of ULVZ material (up to 10%) might prohibit entrainment of the material to the observed scattering heights (Bower et al., 2011). In the vicinity of the LLVP boundaries, it is possible that scattering may occur at the transition between the LLVP material and the ambient mantle, however, the mechanism by which this would occur has not been fully investigated. It is unclear how any of the discussed mechanisms could explain the observed lateral and vertical distribution of small-scale heterogeneities, both inside and outside of LLVPs, as well as the heterogeneity size, as simply as subducted oceanic crust. However, a combination of these sources may be expected, and might explain aspects of the observed scattering.

The distribution of small-scale heterogeneity near LLVP margins is consistent with a thermo-chemical origin of LLVPs (McNamara and Zhong, 2005) with strong radial flow near pile margins that entrains crust up off the CMB (Li et al., 2014) (Supplementary Figs. 7 and 8). Nevertheless, scattering heterogeneities are observed throughout the lower mantle, in regions away from the LLVPs, but in lower abundance. This suggests recycled oceanic crust may be stirred into the mantle, and can retain a seismic signature distinct from background deep mantle material with little apparent deformation over long time periods of 100s of Myrs and greater. These results suggest a connection between small- and large-scale structures through dynamics processes within the lower mantle. Further analysis of scattering heterogeneities throughout the mantle will help to resolve the extent of this connection.

Acknowledgements

This work was supported by NSF grant NSF EAR1401270, and NERC grants NE/K006290/1 and NE/H022473/1. CTBT International Monitoring System data used here were acquired while the author was undertaking a studentship sponsored by the UK National Data Centre at AWE Blacknest.

Appendix A. Supplementary material

Supplementary material related to this article can be found online at <http://dx.doi.org/10.1016/j.epsl.2017.04.036>.

References

- Auer, L., Boschi, L., Becker, T., Nissen-Meyer, T., Giardini, D., 2014. Savani: a variable resolution whole-mantle model of anisotropic shear velocity variations based on multiple data sets. *J. Geophys. Res., Solid Earth*, 1–29.
- Blandford, R.R., 1974. An automatic event detector at the Tonto Forest seismic observatory. *Geophysics* 39, 633–643.
- Bondar, I., North, R.G., Beall, G., 1999. Teleseismic slowness-azimuth station corrections for the International Monitoring System seismic network. *Bull. Seism. Soc. Am.* 89, 989–1003.
- Bower, D.J., Wicks, J.K., Gurnis, M., Jackson, J.M., 2011. A geodynamic and mineral physics model of a solid-state ultralow-velocity zone. *Earth Planet. Sci. Lett.* 303, 193–202.
- Capon, J., Greenfield, R., Kolker, R., 1967. Multidimensional maximum-likelihood processing of a large aperture seismic array. *Proc. IEEE* 55, 192–211.
- Christensen, U.R., Hofmann, A.W., 1994. Segregation of subducted oceanic crust in the convecting mantle. *J. Geophys. Res.* 99, 19,867–19,884.
- Cleary, J., Haddon, R.A.W., 1972. Seismic wave scattering near the core–mantle boundary: a new interpretation of precursors to PKP. *Nature* 240, 549–551.
- Davies, D., Kelly, E.J., Filson, J.R., 1971. Vespa process for analysis of seismic signals. *Nat. Phys. Sci.* 232, 8–13.
- Davies, D.R., Goes, S., Lau, H.C.P., 2015. Thermally dominated deep mantle LLSVPs: a review. In: Khan, A., Deschamps, F. (Eds.), *The Earth's Heterogeneous Mantle*. Springer International Publishing, pp. 441–477. Chap. 14.
- Doornbos, D.J., 1978. On seismic-wave scattering by a rough core–mantle boundary. *Geophys. J. R. Astron. Soc.* 53, 643–662.
- Dziewonski, A.M., 1984. Mapping the lower mantle: determination of lateral heterogeneity in P velocity up to degree and order 6. *J. Geophys. Res.* 89, 5929–5952.
- Earle, P.S., 2002. Origins of high-frequency scattered waves near PKKP from large aperture seismic array data. *Bull. Seismol. Soc. Am.* 92, 751–760.
- French, S.W., Romanowicz, B.A., 2014. Whole-mantle radially anisotropic shear velocity structure from spectral-element waveform tomography. *Geophys. J. Int.* 199, 1303–1327.
- Frost, D.A., Rost, S., Selby, N.D., Stuart, G.W., 2013. Detection of a tall ridge at the core–mantle boundary from scattered PKP energy. *Geophys. J. Int.* 195, 558–574.
- Garnero, E.J., McNamara, A.K., 2008. Structure and dynamics of Earth's lower mantle. *Science* 320, 626–628.
- Grand, S.P., 2002. Mantle shear-wave tomography and the fate of subducted slabs. *Philos. Trans. R. Soc. Lond. A* 360, 2475–2491.
- Grand, S.P., van der Hilst, R.D., Widiyantoro, S., 1997. Global seismic tomography: a snapshot of convection in the Earth. *GSA Today* 7, 1–7.
- Grocholski, B., Catalli, K., Shim, S.-H., Prakapenka, V., 2012. Mineralogical effects on the detectability of the Postperovskite boundary. *Proc. Natl. Acad. Sci. USA* 109, 2275–2279.
- He, Y., Wen, L., 2009. Structural features and shear-velocity structure of the Pacific Anomaly. *J. Geophys. Res.* 114, 1–17.
- Hofmann, A.W., White, W.M., 1982. Mantle plumes from ancient oceanic crust. *Earth Planet. Sci. Lett.* 57, 421–436.
- Hofmeister, A.M., 1999. Mantle values of thermal conductivity and the geotherm from phonon lifetimes. *Science* 283, 1699–1707.
- Houser, C., Masters, G., Shearer, P., Laske, G., 2008. Shear and compressional velocity models of the mantle from cluster analysis of long-period waveforms. *Geophys. J. Int.* 174, 195–212.
- Kaneshima, S., Helffrich, G., 1998. Detection of lower mantle scatterers northeast of the Marianna subduction zone using short-period array data. *J. Geophys. Res.* 103, 4825–4838.
- Kennett, B.L.N., Engdahl, E.R., 1991. Traveltimes for global earthquake location and phase identification. *Geophys. J. Int.* 105, 429–465.
- Knittle, E., Jeanloz, R., 1991. Earth's core–mantle boundary: results of experiments at high pressures and temperatures. *Science* 251, 1431–1443.
- Korenaga, J., 2004. Mantle mixing and continental breakup magmatism. *Earth Planet. Sci. Lett.* 218, 463–473.
- Labrosse, S., Hernlund, J.W., Coltice, N., 2007. A crystallizing dense magma ocean at the base of the Earth's mantle. *Nature* 450, 4–7.
- Lay, T., Hernlund, J., Garnero, E.J., Thorne, M.S., 2006. A post-perovskite lens and D'' heat flux beneath the central Pacific. *Science* 314, 1272–1276.
- Li, C., van der Hilst, R.D., Engdahl, E.R., Burdick, S., 2008. A new global model for P wave speed variations in Earth's mantle. *Geochem. Geophys. Geosyst.* 9, Q05018.
- Li, M., McNamara, A.K., Garnero, E.J., 2014. Chemical complexity of hotspots caused by cycling oceanic crust through mantle reservoirs. *Nat. Geosci.* 7, 366–370.
- Li, M., Black, B., Zhong, S., Manga, M., Rudolph, M.L., Olson, P., 2016. Quantifying melt production and degassing rate at mid-ocean ridges from global mantle convection models with plate motion history. *Geochem. Geophys. Geosyst.* 17, 2884–2904.
- Ma, X., Sun, X., Wiens, D.A., Wen, L., Nyblade, A., Anandkrishnan, S., Aster, R., Huerta, A., Wilson, T., 2016. Strong seismic scatterers near the core mantle boundary north of the Pacific Anomaly. *Phys. Earth Planet. Inter.* 253, 21–30.
- Mancinelli, N., Shearer, P., Thomas, C., 2016. On the frequency dependence and spatial coherence of PKP precursor amplitudes. *J. Geophys. Res.* 121, 1873–1889.
- Mancinelli, N.J., Shearer, P.M., 2013. Reconciling discrepancies among estimates of small-scale mantle heterogeneity from PKP precursors. *Geophys. J. Int.* 195, 1721–1729.
- Masson, D.G., 1991. Fault patterns at outer trench walls. *Mar. Geophys. Res.* 13, 209–225.
- McNamara, A.K., Zhong, S., 2005. Thermochemical structures beneath Africa and the Pacific Ocean. *Nature* 437, 1136–1139.
- Moresi, L., Gurnis, M., 1996. Constraints on the lateral strength of slabs from three-dimensional dynamic flow models. *Earth Planet. Sci. Lett.* 138, 15–28.
- Moulik, P., Ekstrom, G., 2014. An anisotropic shear velocity model of the Earth's mantle using normal modes, body waves, surface waves and long-period waveforms. *Geophys. J. Int.* 199, 1713–1738.
- Murakami, M., Hirose, K., Kawamura, K., Sata, N., Ohishi, Y., 2004. Post-perovskite phase transition in MgSiO_3 . *Science* 304, 855–858.
- Obayashi, M., Yoshimitsu, J., Nolet, G., Fukao, Y., Shiobara, H., Sugioka, H., Miyamachi, H., Gao, Y., 2013. Finite frequency whole mantle P wave tomography: improvement of subducted slab images. *Geophys. Res. Lett.* 40, 5652–5657.
- Oganov, A.R., Ono, S., 2004. Theoretical and experimental evidence for a post-perovskite phase of MgSiO_3 in Earth's D'' layer. *Nature* 430, 445–448.
- Olson, P., Yuen, D.A., Balsiger, D., 1984. Mixing of passive heterogeneities by mantle convection. *J. Geophys. Res.* 89, 425–436.
- Ritsema, J., Deuss, A., van Heijst, H.J., Woodhouse, J.H., 2011. S40RTS: a degree–40 shear-velocity model for the mantle from new Rayleigh wave dispersion, teleseismic traveltimes and normal-mode splitting function measurements. *Geophys. J. Int.* 184, 1223–1236.
- Rost, S., Earle, P.S., 2010. Identifying regions of strong scattering at the core–mantle boundary from analysis of PKKP precursor energy. *Earth Planet. Sci. Lett.* 297, 616–626.
- Selby, N.D., 2008. Application of a generalized F detector at a seismometer array. *Bull. Seismol. Soc. Am.* 98, 2469–2481.
- Shearer, P.M., 2007. Deep Earth structure seismic scattering in the deep Earth. In: Schubert, G. (Ed.), 1st edn. In: *Treatise on Geophysics*, vol. 1. Elsevier B.V., pp. 695–729.
- Shearer, P.M., Earle, P.S., 2004. The global short-period wavefield modelled with a Monte Carlo seismic phonon method. *Geophys. J. Int.* 1103–1117.
- Simmons, N.A., Forte, A.M., Boschi, L., Grand, S.P., 2010. GyPSuM: a joint tomographic model of mantle density and seismic wave speeds. *J. Geophys. Res.* 115, 1–24.
- Stracke, A., Bizimis, M., Salters, V.J.M., 2003. Recycling oceanic crust: quantitative constraints. *Geochem. Geophys. Geosyst.* 4.
- Tackley, P., 2011. Living dead slabs in 3-D: the dynamics of compositionally-stratified slabs entering a “slab graveyard” above the core–mantle boundary. *Phys. Earth Planet. Inter.* 188, 150–162.
- Thorne, M., Garnero, E.J., Grand, S.P., 2004. Geographic correlation between hot spots and deep mantle lateral shear-wave velocity gradients. *Phys. Earth Planet. Inter.* 146, 47–63.
- Williams, C.D., Li, M., McNamara, A.K., Garnero, E.J., Soest, M.C.V., 2015. Episodic entrainment of deep primordial mantle material into ocean island basalts. *Nat. Commun.* 6, 1–7.
- Williams, Q., Garnero, E.J., 1996. Seismic evidence for partial melt at the base of Earth's mantle. *Science* 273, 1528–1530.